High-temperature ex-vessel corium spreading. Part 1: Experimental investigations on ceramic and sacrificial concrete substrates.

Michael Johnson, Arthur Denoix, Viviane Bouyer, Hiroshi Goda, Satoru Kamohara, Junichi Takeuchi, Laurent Brissonneau, Christophe Journeau

High-temperature ex-vessel corium spreading. Part 1: Experimental investigations on ceramic and sacrificial concrete substrates.

M. Johnson[a], A. Denoix[a], V. Bouyer[a], H. Goda[b], S. Kamohara[b],J. Takeuchi[b], L. Brissonneau[c] and C. Journeau[a]

[a]CEA, DES, IRESNE, DTN, SMTA, LEAG, Cadarache, 13115 Saint-Paul-lez-Durance, France
[b]Mitsubishi Heavy Industries, Ltd., Reactor Core Safety Engineering Department, Nuclear Energy Systems Division, Kobe, Japan
[c]CEA, DES, IRESNE, DTN, SMTA, LMCT, Cadarache, 13115 Saint-Paul-lez-Durance, France

ARTICLE HISTORY
Compiled July 30, 2021

ABSTRACT
Optimizing melt spreading in the aftermath of a core disruptive accident is crucial for achieving sufficient melt cooling to maintain reactor containment integrity. Two $\approx$ 30 kg-scale experiments performed at the VULCANO facility explore the spreading of high-temperature molten corium-concrete mixtures over ceramic and sacrificial concrete substrates. Imaging of the melt front propagation revealed a 7 % increase in spreading length and a 30 % increase in maximum front velocity during spreading over sacrificial concrete, despite a reduced mass partaking in spreading due to increased holdup within the crucible. Infrared imaging of the melt indicated surface temperatures around 45 °C lower during spreading on sacrificial concrete, which is anticipated to result in a roughly three-fold increase in melt viscosity. The 7 % observed increase in spreading length therefore likely underestimates the extent of the increase in melt *spreadability* on sacrificial concrete, given the reduced mass and increased melt viscosity apparent during the VE-U9-concrete test. The enhanced spreadability on sacrificial concrete could be explained by the apparent *gliding* motion of the melt, combined with the shallower melt profile towards the spreading front, which are consistent with reduced friction at the melt-substrate interface. Reduced friction at the melt-substrate interface is best explained by a diphasic film of molten concrete and gases generated by the molten core-concrete interaction acting as a lubricant between the melt and solid substrate.

KEYWORDS
severe accident; ex-vessel; corium; spreading

1. Introduction

A fundamental principle of nuclear safety is that the integrity of the reactor containment must be preserved in the aftermath of a severe accident, such that any consequences are limited to the site itself[1,2]. A hypothetical severe accident scenario considers a core meltdown, relocation of high-temperature lava-like mixtures of molten nuclear fuel and reactor components (corium) and breach of the reactor pressure vessel

CONTACT C. Journeau. Email: Christophe.Journeau@cea.fr

(RPV)[3]. On failure of the RPV, the high-temperature corium will impinge on the containment floor, or core catcher, resulting in a combination of surface ablation[4] and spreading over a designated area of sacrificial concrete[1,2]. Maintaining containment integrity requires that the ablation depth remains lower than the thickness of the sacrificial concrete layer, which requires substantial cooling of the molten corium. Lateral spreading enhances the melt heat transfer area and thus its coolability, while also dissipating the thermal load on the containment floor. Promoting ex-vessel corium spreading over a broad area, forming a thin layer of enhanced coolability, therefore represents a key strategy for maintaining containment integrity in contemporary core catcher designs, such as for the EPR and ATMEA1[5].

For viscous corium melts, the spreading dynamics are likely to be largely dictated by a balance of gravitational and viscous forces[6]. The melt temperature evolves with time due to the radioactive decay heat, conductive heat transfer from the melt to the substrate and the thermal radiation and free convection heat losses from the free surface of the melt. If the thermal losses exceed the heat generation due to radioactive decay the melt will eventually undergo solidification at the surface and the melt-substrate interface, leading to crust formation[3,7]. The viscous resistance to flow increases exponentially with the melt solid fraction[1,8] and spreading may be arrested altogether if the immobilization solid fraction[1] is attained. Prior to immobilization the flow may become increasingly controlled by the deformation mechanics and fracturing of the solid crust layer[3,9,10].

Interaction of the high-temperature melt with the sacrificial concrete introduces additional considerations likely to impact the spreading dynamics[2]. The molten core-concrete interaction (MCCI)[11] generates gases (notably steam and hydrogen), which percolate through the melt, diminishing the bulk density but also potentially accentuating the rate of heat loss[2,12,13] by effectively *sparging* the melt. The mixture of corium with concrete decomposition products has also been observed to result in significant reductions in solidus and liquidus temperatures[14]. The competition between the sparging effects and the reduction in solidus and liquidus temperatures is unclear, rendering the rate of crust growth and the attainment of the immobilization condition highly uncertain. The formation of a gaseous film or liquid film, rich in molten concrete, may also enhance slip at the melt-concrete interface[15]. The slip condition is likely to impact the velocity profile and structure, or topology, of the melt, with no-slip cases often characterised by an *elevated nose*, whereby the most advanced point of the melt front is suspended above the substrate[15]. Direct numerical simulations have indicated that increased friction at the melt-substrate interface substantially retards the front propagation for low-moderate Reynolds number flows[15].

A number of experimental investigations of high-temperature melt spreading, over both wet and dry substrates, have been performed to date[2]. Japanese SPREAD tests of thermite-steel melts spreading on concrete implied immobilization solid fractions in the order of 55 %[16]. The VULCANO VE-U7 spreading test on concrete[1] demonstrated virtually isothermal spreading until the spreading front had almost arrested and thus spreading was not determined to be limited by heat transfer effects. Conversely, during the KATS experiments[17], the spreading length was reduced from 11 m on ceramic to 7 m on concrete. This was considered to be a consequence of the MCCI sparging effects enhancing the rate of melt cooling, manifesting in a four-fold increase in bulk viscosity within the timescale of spreading[2,17]. Experiments at the FARO facility[18] implied radiation losses from the melt free surface to be particularly significant in immobilizing the melt front.

The following investigation presents two < 50 kg-scale spreading tests of molten

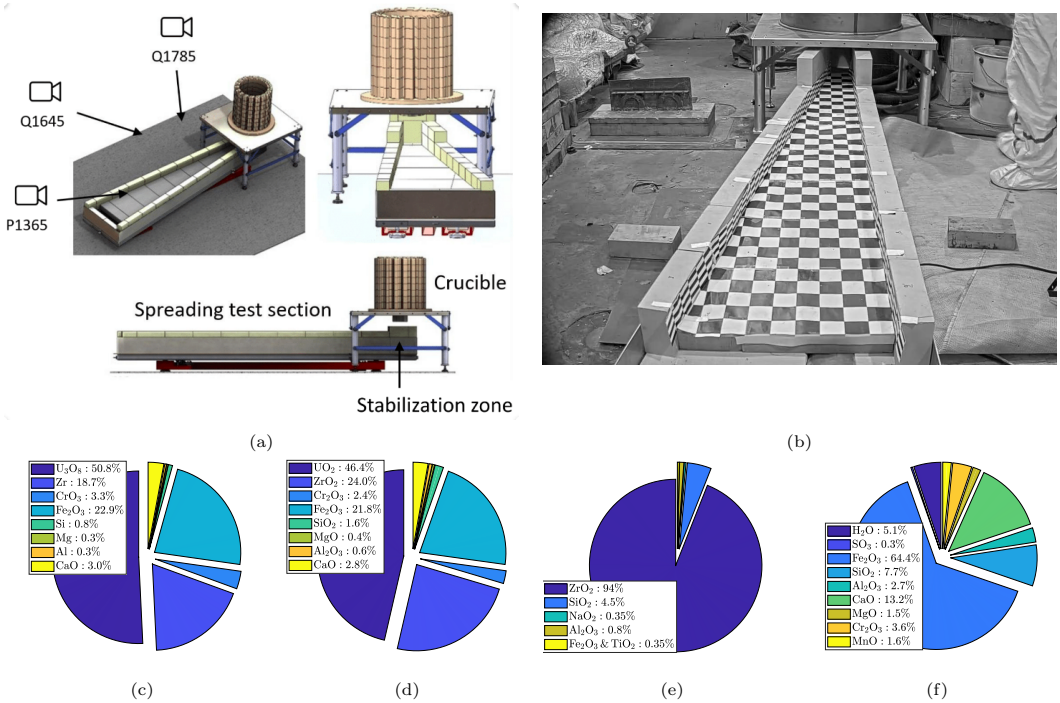

Figure 1. (a) Schematic of the VULCANO test facility as configured for the VE-U9 spreading tests, (b) a checkerboard calibration image of the spreading section (the black and white squares measure 5×5 mm), and the chemical compositions of the corium-concrete-thermite mixture (c) pre- and (d) post-combustion, and of the (e) ceramic and (f) sacrificial concrete substrates.

core-concrete mixtures on ceramic (VE-U9-ceramic) and sacrificial concrete (VE-U9-concrete) substrates at the CEA's VULCANO facility[19]. The spreading test on refractory ceramic ensures an inert interaction at the melt-substrate interface, providing a control case for establishing the influence of the MCCI on the spreading dynamics on concrete. Spreading dynamics are interpreted with the aid of optical and infrared video imaging of the spreading and real-time monitoring of the melt mass discharged into the spreading channel.

2. Materials and Methods

Two < 50 kg-scale spreading tests (VE-U9) were performed at the CEA's VULCANO facility, a schematic of which is presented in Figure 1a. The facility consists of a 305 mm diameter crucible with a 60 mm hole at the base, mounted on a table with a 120 mm hole at its centre. The crucible is constructed of zirconia bricks and is housed within a steel casing with a sand-filled cavity between the zirconia and steel. Melt discharge is controlled by the melting of a 3 mm thick tin plug covering the hole at the base of the crucible. The crucible is mounted above a stabilization zone, which regulates the melt flow into the spreading channel. The spreading channel and stablization zone are walled with zirconia bricks. The entry to the spreading channel is 95 mm wide, with walls diverging at an angle of 9.5° along its 2 m length. Consistent with the VE-U7 spreading test[19], the two spreading channel geometries represent mirror images of each other, however these tests were performed sequentially, whereas the VE-U7 tests were performed concurrently, on adjacent channels, beneath a shared crucible.

The melt load consists of a prototypic corium-concrete-thermite mixture, the melting of which was driven by a highly exothermic thermite reaction. The thermite reaction was ignited by a aluminum-ruthenium wire heating the mixture to local temperatures in the order of 2000 °C. Within the reaction mixture, chromium and iron oxides (CrO_3 and Fe_2O_3) act as the primary oxidisers, with zirconium as the principal reducer, while hyperstoichiometric uranium oxide (U_3O_8) provides a supplementary oxygen source, reducing to UO_2. The composition of the load and the theoretical composition after combustion are presented in Figure 1c and d respectively.

For the VE-U9-ceramic test, the basemat of the spreading channel was constructed of 50 mm deep fused zirconia bricks (Saint Gobain - SEFPRO, France), the composition of which is detailed in Figure 1e. The VE-U9-concrete test was performed using a basemat constructed of 50 mm deep slabs of sacrificial concrete, prepared according to a recipe provided by Mitsubishi Heavy Industries (MHI). The sacrificial concrete composition, detailed in Figure 1f, has a high iron content aimed at diminishing the liquidus temperature and reducing the viscosity in the molten phase compared to silica-rich concretes, while also avoiding the quantity of gas production associated with limestone-rich concretes.

2.1. In situ instrumentation

The spreading channel was mounted on three 300 ± 0.051 kg scales (Scaime, France) to detect the rate of mass flow onto the test section. Three HD cameras (models Q1645, Q1785 and P1365, Axis Communications, Sweden), installed within protective housings, were used to acquire videos of the melt spreading from the different perspectives indicated in Figure 1a, capturing the melt progression at frame rates of 15–50 fps. A more precise specification of the camera perspectives is obtained from image analysis (see Section 2.1.1) of the checkerboard calibration images such as that presented in Figure 1b. Two additional ceiling cameras (Dome 1 and 2, Axis Communications, Sweden) acquired videos from above the crucible to observe the melting and initial melt discharge. Optical imaging was supplemented by infrared imaging of the melt progression, for an enhanced understanding of the evolution of surface temperature. Infrared images were acquired using a MIKRON MCS640 camera (Advanced Energy, USA) configured with a measurement range of 739–3136 °C.

Inconel alloy sheathed Type K thermocouples, with a detection range of 0–1300 °C, were used to monitor heat transfer to the substrates at various locations; 18 such thermocouples were embedded at the joints between the zirconia bricks during the VE-U9-ceramic test, while 34 were embedded within the concrete for the VE-U9-concrete test. Molybdenum and Inconel sheathed type C thermocouples, with an elevated detection range of 400–2300 °C, were installed within the stabilization zone (at depths of between 2 mm beneath and 20 mm above the surface) to monitor the evolution in melt temperature prior to arrival at the spreading channel. The temperature within the stabilization zone was also monitored using a video pyrometer (Keller ITS, Germany) with a temperature range of 850–3000 °C.

2.1.1. Image calibration

Checkerboard calibration images[19] were obtained from each camera perspective after covering the floor of the channel with 50×50 mm black and white squares and the boundary walls with 10×50 mm rectangles (see Figure 1b). The corners, or nodes, of these checkerboard images were detected[20], transformed to square coordinates con-

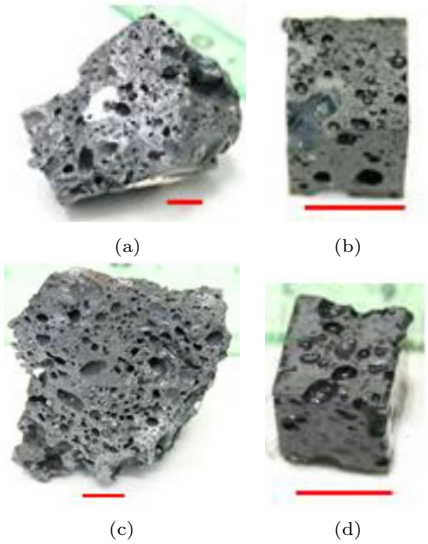

Figure 2. Samples extracted from the solidified melts of (a) VE-U9-ceramic and (c) VE-U9-concrete and their corresponding cubic sub-samples in (b) 3b-2 and (d) 2b-3 respectively, extracted for density and porosity analysis; the scale bars are 10 mm in length.

sistent with a birds-eye view[21,22] and interpolated[23] to obtain a calibration map of the real physical coordinates corresponding to each pixel within the spreading test section. The melt contours were then segmented from the videos by dynamic thresholding and then translated to real coordinates using the calibration maps. Image processing was performed using SPECTRA (Software for Phase Extraction and Corium TRacking Analysis)[24], an image analysis application built using Matlab 2018b (MathWorks, USA).

2.2. Dismantling, sampling and post-test analysis

At the end of each spreading test, and once the melt had cooled to ambient temperature, the final spreading length was measured from the entry to the spreading channel (along the central axis between the channel walls) and the depth of the melt along its central axis was recorded at regular intervals. The solidified melt was then dismantled and weighed to determine the mass distribution of melt (1) remaining in the crucible, (2) held up within the stabilization zone prior to the spreading channel (see Figure 1a), and (3) as a function of distance along the length of the spreading channel.

Samples were excavated from the solidified melt (see Figure 2a and c) and their sampling locations recorded. The samples are labelled according to a qualitative classification of their sampling location. The length (x) locations of the samples were classified as zones 1-4. Zone 1 corresponds to the stabilization zone prior to the spreading channel, while the melt within the spreading channel was divided into three thirds (zones 2-4) corresponding to the channel entry, middle and front regions respectively. The depth classifications are assigned as (a) close to the melt-substrate interface, (b) intermediate and (c) close to the free surface. Cubic sub-samples of $\approx$1 cm^3 volume (see Figure 2b and d) were cut from the larger samples for subsequent porosity and density analysis.

2.2.1. Density and porosity analysis

The density and the open and closed components of porosity were determined for each sample using a MS-DYN-43 density kit (Mettler-Toledo, USA). The mass of a sample is measured to $\pm 10^{-4}$ g precision in both air and ethanol, enabling the estimation of the sample volume, exclusive of open pores, using Archimedes' principles. The masses in air and ethanol are determined for three, or i, different forms (or preparation methods) of each sample, corresponding to (1) the untreated sample, (2) the sample with its open pores impregnated under vacuum with Epofix epoxy resin (Struers, Denmark), and (3) the sample milled into a powder and remolded in epoxy resin. The mass of added resin is recorded in the case of forms 2 and 3 and is denoted $m_{i,res}$ (where $i \in 2, 3$). The masses in air and ethanol of each of the 3 forms of the sample, the mass of added resin for forms 2 and 3, and the known densities of air, ethanol and resin are used to determine the open, ϕ_o, and closed, ϕ_c, components of the porosity. The relevant relationships for this density and porosity characterization are provided in Appendix A.

3. Results and discussion

3.1. Post-test observations

Images of the cooled, solidified melt at the conclusion of the spreading tests are presented in Figure 3a-b. The final spreading lengths measured 0.635 m on ceramic and 0.680 m on sacrificial concrete, representing a 7 % increase in spreading length on concrete (note that potential disparities in spreading mass, viscosity and porosity between the tests must be characterized and scaled for before comparing the two spreading lengths). The VE-U9-ceramic test presented with a thin melt layer of around 10 mm thickness, extending a distance of $\approx$ 150 mm from one corner of the melt front (as observed in the bottom corner of Figure 3a), which shall be referred to as the melt *tongue*. Since the mass of this tongue is negligible in comparison with the body of the melt, the tongue was not included in the measurement of the effective spreading length.

The melt was punctuated by silvery-white metallic inclusions, as observed in Figure 3a and perhaps more clearly in the samples shown in Figure 2. The magnetic behaviour of these inclusions revealed them to be rich in metallic iron (consistent with observations from the previous VF-U1 corium-concrete interaction at the VULCANO facility[25]), generated by the reduction of iron oxide during the corium-thermite reaction. The predicted post-combustion melt composition shown in Figure 1d was calculated on the assumption that the high-temperature reaction mixture would be sufficiently exposed to ambient oxygen for the metallic iron to fully re-oxidise to Fe_2O_3, however this re-oxidation reaction does not appear to proceed to completion.

Depth measurements along the length of the cooled melt after the termination of spreading, presented in Figure 3c, revealed a difference in the topology. The VE-U9-ceramic melt exhibited greater depth close to the entry to the spreading channel and a more severe curvature at the spreading front, whereas the VE-U9-concrete melt was characterised by a shallower nose and a more linear profile between the source the front. Neither melt profile clearly exhibited a distinctive overhang at the melt front, or *elevated nose*, consistent with some simulations of melt spreading under no-slip conditions[15]. The steeper melt profile at the spreading front on the zirconia substrate is consistent with enhanced resistance to spreading at the melt-substrate

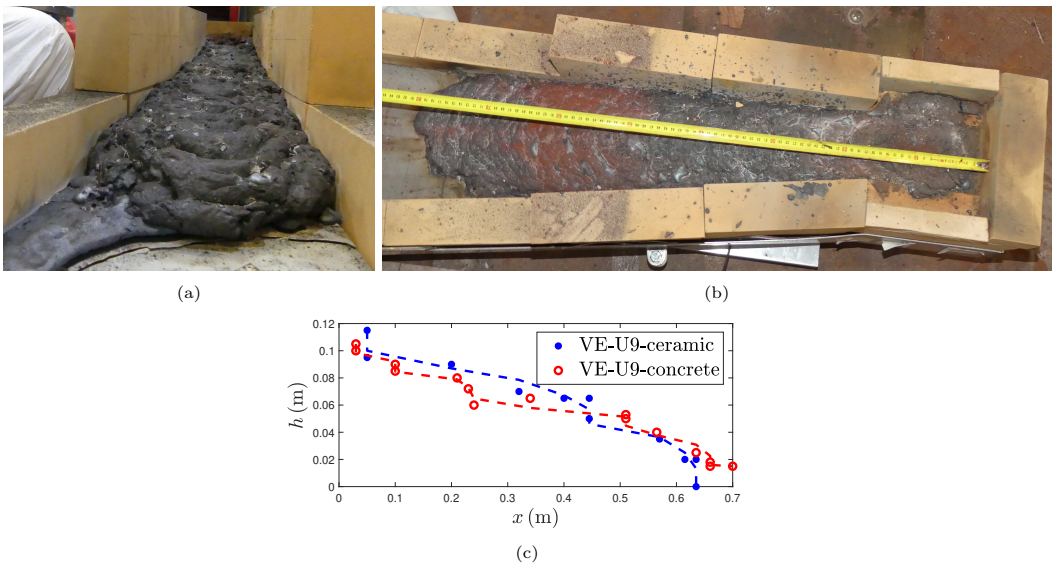

Figure 3. Images of the cooled melt following the (a) VE-U9-ceramic and (b) VE-U9-concrete tests and (c) the melt profiles at the end of experimentation from local depth measurements taken during dismantling (the dashed lines represent moving averages of the local measurements to aid the visualisation of the profiles).

interface. The high-friction at the melt-substrate interface manifests in a significant disparity between the melt velocity at the free surface and the diminished velocity at the melt-substrate interface, which forces the melt to advance with a *crawling* motion (picture the motion of the tread of *continuous-track* vehicles, such as an armoured tank or snowmobile), resulting in a steeper profile at the front than low-friction cases characterized by a *gliding* motion.

Ahead of the spreading fronts burn marks were apparent on the sacrificial concrete but not on the zirconia substrate. Following the dismantling of the VE-U9-concrete test and removal of the solidified melt, certain thermocouples, embedded at depths of 2 mm within the concrete prior to experimentation, were exposed at the surface, indicating ablation of the sacrificial concrete basemat. The fact that other thermocouples at equivalent depths remained concealed below the surface indicates that the MCCI caused local ablation to depths of up to 2–4 mm. As anticipated, there was no evidence of chemical or thermal damage to the refractory ceramic substrate. Ablation of the sacrificial concrete substrate, but not the refractory zirconia, is likely to contribute to a disparity in slip-behaviour at the melt-substrate interface between the VE-U9 tests.

While the two experiments were configured with the same initial conditions, with the exception of the substrate material, perfect repeatability in experimental conditions is difficult to achieve with high-temperature corium melts. Subtle differences in the mass partaking in spreading, the duration and rate of melt discharge to the spreading channel, the evolution of porosity and temperature, and thus viscosity, of the melt may all significantly influence the spreading dynamics. The observed 7 % increase in spreading length on sacrificial concrete cannot be interpreted without the context of any such differences in these key properties. These parameters will be characterised for the two experiments in the following sections, while the influence of these melt characteristics on the scaling of spreading length will be investigated in part two of this research[26].

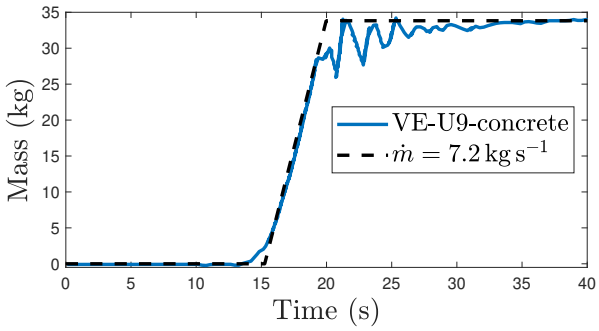

Figure 4. The evolution of mass discharged into the spreading channel and stabilization zone from the crucible during the VE-U9-concrete spreading test.

3.2. Melt mass distribution and flow rate into the channel

The mass distributions of melt at the end of the experiments are detailed in Table 1. In both instances several kilograms of melt remained held up within the crucible, however 16.0 kg of melt remained in the crucible during the VE-U9-concrete test, as compared with 11.3 kg for VE-U9-ceramic. A further 7–7.9 kg was held up within the stabilization zone prior to the start of the spreading section in each instance. Consequently, 31.6 kg of melt was discharged to the ceramic spreading channel, as opposed to 26.0 kg in the case of VE-U9-concrete. The 7 % increase in spreading length on the concrete substrate is therefore likely to underestimate the disparity in *spreadability* on the two substrates, given the 18 % reduction in mass partaking in the spreading on concrete.

Table 1. Melt mass distributions at the end of the spreading tests.

VE-U9-ceramic		VE-U9-concrete	
Location	Mass (g)	Location	Mass (g)
Crucible wall	1925		5989
Crucible floor	6755		9425
Crucible dust	2600		584
Stabilisation pool	7012		7901
0–50 mm	2116	0–20 mm	1528
50–180 mm	4674	20–120 mm	3839
180–240 mm	5503	120–240 mm	4210
240–300 mm	1450	240–340 mm	4000
300–400 mm	3537	340–500 mm	5000
400–470 mm	3842	500–680 mm	2700
470–635 mm	3814		
Dust in test section	710		1557
Samples	5966		3126
Total	49903		49859
Total in spreading channel	31612		25960

The scales supporting the test section malfunctioned during VE-U9-ceramic, but successfully recorded the mass flow onto the test section during VE-U9-concrete. The melt flow onto the concrete channel, inclusive of the stabilization zone, is presented in Figure 4. The final mass of around 32.9 kg is in reasonable agreement with the total mass of 33.9 kg of melt recovered from the test section and stabilization zone post-test, as detailed in Table 1. Around 85 % of the melt is discharged onto the test section

within a period of 5.5 s. The bulk of the melt appears to be discharged at a flow rate of around $7.2\,\mathrm{kg\,s^{-1}}$, with slower flow rates at the start and end of discharge, consistent with a broadly Gaussian profile of melt flow rate, however the melt flow can be crudely approximated by a constant flow rate of $7.2\,\mathrm{kg\,s^{-1}}$ for around 4.58 s, as indicated by the dashed black line in Figure 4. While it is clear that a lower total mass is discharged to the sacrificial concrete channel, there is inadequate evidence to suggest a significant difference in the duration of melt discharge to the two test sections. The duration of spreading will be readdressed during video analysis of the melt spreading dynamics.

3.3. Post-test porosity and density analysis

Porosity analysis is presented for 15 samples recovered from the cooled melt after the VE-U9-ceramic test, and 13 samples from the VE-U9-concrete test in Figure 5. The samples were prepared and labelled as described in Section 2.2. For all samples, the open pores contribute the bulk of the the total porosity. Wide ranging porosities of 23–44 % are observed, with significant local variation in the porosity of samples retrieved from the same location. The heterogeneity in porosity demonstrated no correlation with the sampling location, either with respect to sampling depth or distance from the entry to the spreading channel.

The mean porosity from the VE-U9-ceramic samples of 35.3 ± 4.7 % was slightly greater than that of 29.8 ± 4.3 % for the VE-U9-concrete samples. The slightly increased porosities for the VE-U9-ceramic spreading test on ceramic are perhaps counter-intuitive, since the interaction at the melt-ceramic interface is inert whereas a potential MCCI at the concrete substrate is liable to liberate steam, hydrogen and other gaseous concrete decomposition products[11]. Images from the above the crucible prior to spreading demonstrate significant smoke generation during the thermite reaction which would explain an elevated melt porosity prior to the initial discharge onto the spreading channels. The presence of large void fractions in prototypic corium during spreading over an inert substrate has been reported for previous VULCANO tests[19]. This could be attributed to the significant vaporization of, in particular, uranium oxides, observed for high-temperature corium-concrete mixtures[27]. The diminished porosity in the presence of augmented gas generation at the melt-substrate interface could be explained by sparging of the melt by gas liberated from the concrete, providing channels for continuous gas release. Equally, if the steam percolating through the melt causes the melt to exceed its maximum porosity limit, the melt could initially swell before collapsing under its own weight. In the latter case, the video imaging should demonstrate a cyclical swell and collapse of the melt during spreading on sacrificial concrete.

The porosity analysis also revealed the solidified melt density (exclusive of porosity), which is presented as a function of distance from the start of the spreading test section in Figure 5b. Densities of $6.82 \pm 0.22\,\mathrm{g\,cm^{-3}}$ and $6.63 \pm 0.16\,\mathrm{g\,cm^{-3}}$ were determined for the VE-U9-ceramic and VE-U9-concrete experiments respectively. The 3 % difference in solid melt density between the experiments, and the heterogeneity between samples, has only a minor influence on the bulk melt density as compared with the influence of porosity. The local variation in density is anticipated given the relatively small $1\,\mathrm{cm^3}$ samples, the complex chemical composition of the corium-concrete-thermite reactant mixture and the heterogeneity of the post-combustion metallic inclusions observed in Figure 2.

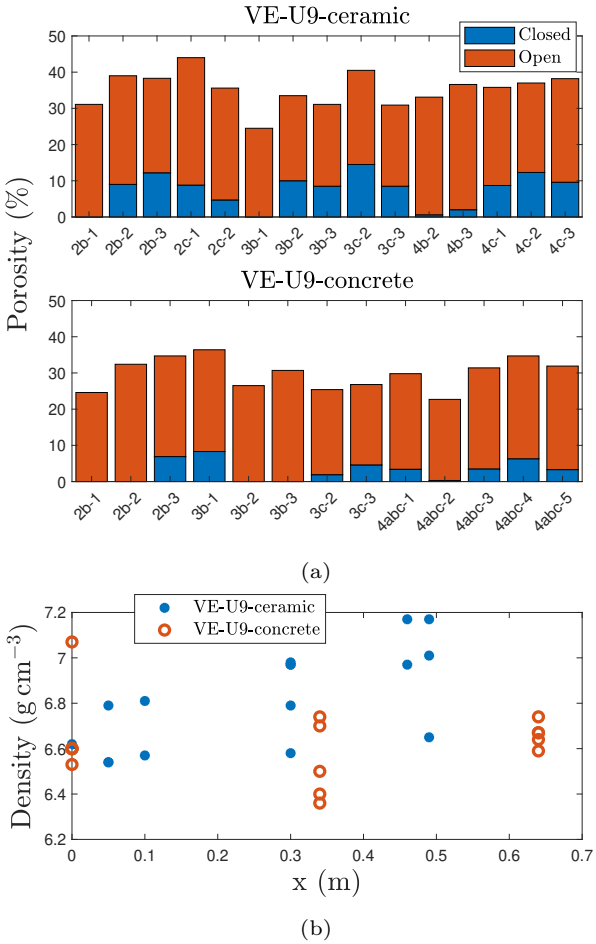

Figure 5. Analysis of (a) the open and closed porosity and (b) the density of the gas-free solid phase for samples retrieved after the completion of the spreading tests.

3.4. Thermal (infrared) image analysis

An example contour plot of melt surface temperature, from infrared thermal imaging of the VE-U9-ceramic test, is presented in Figure 6a, with temperature analysis of profiles along the central axis of the melt (see the red line in Figure 6a) presented in Figure 6b-c. The emissivity of corium-concrete mixtures in the infrared spectrum is not well-characterized and so analysis will be conducted on the basis of an assumed emissivity of 0.8[1], however sensitivity analysis will be presented for estimates in the range of 0.6-1.

From Figure 6a, captured 4.6 s after the first melt sighting in the stabilization zone, the melt exhibits surface temperatures predominantly in the 1800–1850 °C range, with small hotspots closer to 1900 °C, diminishing to a temperature of around 1700 °C at the melt front. The heterogeneity in surface temperature can be seen in the local variance in temperature along the length of the melt in Figure 6b-c. Within the stabilization zone ($x < 0$), the melt surface temperature appears relatively stable during the initial 4 s of melt spreading and cools at a rate of around 40 °C s^{-1} thereafter. The temperature profiles along the melt axis demonstrate the thermal gradient along the length of the melt, whereby the surface temperatures appear around 100 °C lower at the melt

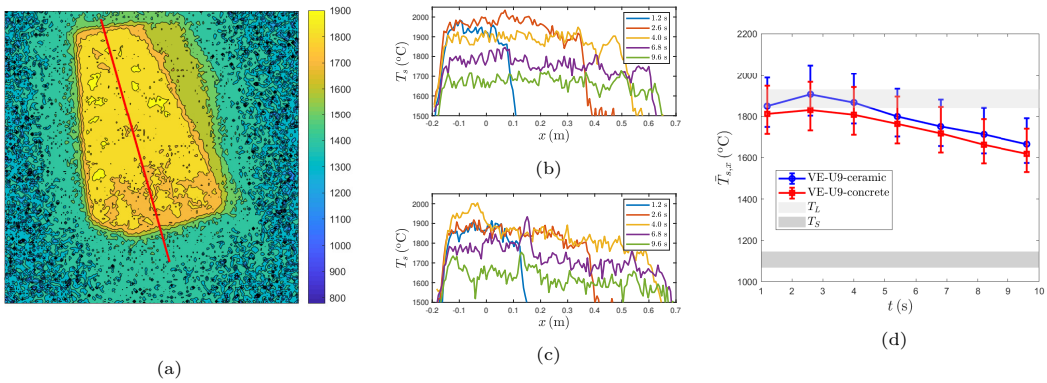

Figure 6. Infrared image analysis of surface temperature including (a) an example contour plot of surface temperatures during the VE-U9-ceramic spreading test (4.6 s after the first melt sighting in the stabilization zone), (b-c) the evolution of surface temperature with time and distance from the start of the spreading section (along the red analysis line in (a)) during the (b) VE-U9-ceramic and (c) VE-U9-concrete spreading tests (note that $x < 0$ corresponds to the stabilization zone), and (d) the evolution of spreading length averaged surface temperatures during the two tests, the error bars indicate the sensitivity of surface temperature to a ± 0.2 uncertainty in emissivity and the grey shaded areas represent the anticipated solidus and liquidus temperatures for the corium-concrete mixture.

front than at the entry to the spreading channel ($x = 0$).

Surface temperatures, averaged along the length of the melt, $\bar{T}_{s,x}$, are presented in Figure 6d. The error bars indicate surface temperature estimates corresponding to emissivity values of 0.6 and 1. The length averaged surface temperatures for both experiments appear relatively stable during the initial 4 s of spreading, diminishing at a rate of around 30–40 °C s^{-1} thereafter, mirroring the evolution of temperature within the stabilization zone. The slight rise in surface temperature around 2.6 s after the initial melt arrival during VE-U9-ceramic may simply reflect the significant melt cooling on first contact with the substrate within the stabilization zone, which becomes less apparent once a larger thermal mass is discharged from the crucible. Since Figure 4 indicated that 85 % of the melt discharged to the concrete channel occurred within a period of 5.5 s, the bulk of the melt discharge occurs on a timescale of minimal evolution in the length-averaged melt surface temperature. Conversely, the 100 °C drop in temperature along the spreading length indicates that the viscous resistance may be significantly greater at the front than close to the entry to the spreading channel.

Interpretation of the infrared analysis of melt temperature and its implications for bulk viscosity requires three caveats, (1) surface temperature estimates will underestimate the bulk melt temperature, (2) temperature estimates are subject to the uncertainty in melt emissivity, and (3) the viscosity of corium-concrete mixtures is not yet well characterized as a function of temperature. However, assuming the melt emissivity to be insensitive to temperature and thus comparable for the two tests (which share identical corium load compositions), it appears that the melt surface temperatures are in the order of 45 °C lower during spreading on sacrificial concrete. Assuming an emissivity value of 0.8, the length averaged surface temperatures appear to be comparable in magnitude to, or slightly lower than, the estimated range of liquidus temperatures[14], shaded in light grey in Figure 6d, indicating that some solidification is likely at the free surface. Conversely, even for the black body assumption ($\epsilon = 1$), corresponding to the lowest estimate for surface temperature (see the lower bound of the error bars in Figure 6d), temperatures exceed the solidus temperatures by 400–600 °C. It is anticipated that surface temperatures closer to the estimated solidus

would be required for sufficient melt solidification to form a continuous crust.

Further investigation of melt solidification between the solidus and liquidus temperatures, and improved characterisation of corium viscosity, are required, and so the influence of a $\approx 45\,^{\circ}\mathrm{C}$ difference in melt surface temperature between the two experiments on viscosity is not easily quantified. However, the temperature dependence of the viscosity of pure corium is often represented by equations in the form[1,28]:

$$\mu = \mu_L \, e^{k_\mu (T - T_L)} \tag{1}$$

where μ_L is the viscosity at the liquidus temperature and values for the exponential coefficient, k_μ, have been proposed for corium in the order of $-0.0287 < k_\mu < -0.0201$[1]. Coefficients of this magnitude would indicate that a reduction in melt temperature by $45\,^{\circ}\mathrm{C}$, in the case of spreading on concrete, would correspond to an increase in viscosity by a factor of 2.5–3.6 . Equally, cooling rates of $\approx 35\,^{\circ}\mathrm{C\,s^{-1}}$ in the later stages of melt spreading would imply a doubling of viscosity every 0.7–1.0 s. Most significantly, exponential coefficients of this magnitude would indicate that a $100\,^{\circ}\mathrm{C}$ temperature drop along the spreading length would result in a viscosity 7–17 times greater at the front than at the entry to the spreading channel.

The roughly three-fold increase in average viscosity and an 18 % reduction in the total mass partaking in the spreading both imply a reduced spreading potential for the VE-U9-concrete test, in contrast to the observed 7 % increase in spreading length. Video imaging analysis of the evolution of the melt flow is employed to investigate this disparity in spreading dynamics between the two tests.

3.5. Optical image analysis

An example image, acquired from the Q1645 camera perspective during the VE-U9-ceramic test, is presented in Figure 7a. The melt phase was segmented from each video frame and melt contours were translated to physical coordinates, using the checkerboard calibration image in Figure 1b, according to the method outlined in Section 2.1.1. The primary obstacles during the segmentation and calibration process were (1) the halo of glare surrounding the melt phase, complicating the precise detection of melt border, (2) the heterogeneity of luminosity over the melt surface, consistent with that observed from the thermal imaging, and (3) the poor illumination of the start of the spreading section in the calibration image due to shading by the crucible. These factors were considered to result in a ± 50 mm uncertainty in the melt footprint contours presented in Figure 7c-d.

Image analysis indicated final spreading lengths, $x_{N,f}$, of 0.65 and 0.71 m for the VE-U9-ceramic and VE-U9-concrete tests respectively, demonstrating acceptable agreement with the lengths of 0.635 and 0.68 m from post-test measurements of the solidified melt. The melt fronts propagated during a period of around 6–8 s, after which spreading on both substrates arrested or slowed to a negligible velocity, which is consistent with the duration of melt discharge from the crucible to the concrete channel in Figure 4. The emergence of the tongue is observed between the contours at 16 and 33 s in Figure 7bb, after melt spreading appeared to have arrested on the ceramic substrate. The tongue is best explained by the breach of a crust at the melt front by high-temperature melt, thereby instigating a brief period of secondary spreading. This is supported by the increased luminosity of the tongue, seen in the bottom left corner of Figure 7a, indicating a greater bulk melt temperature beneath the surface.

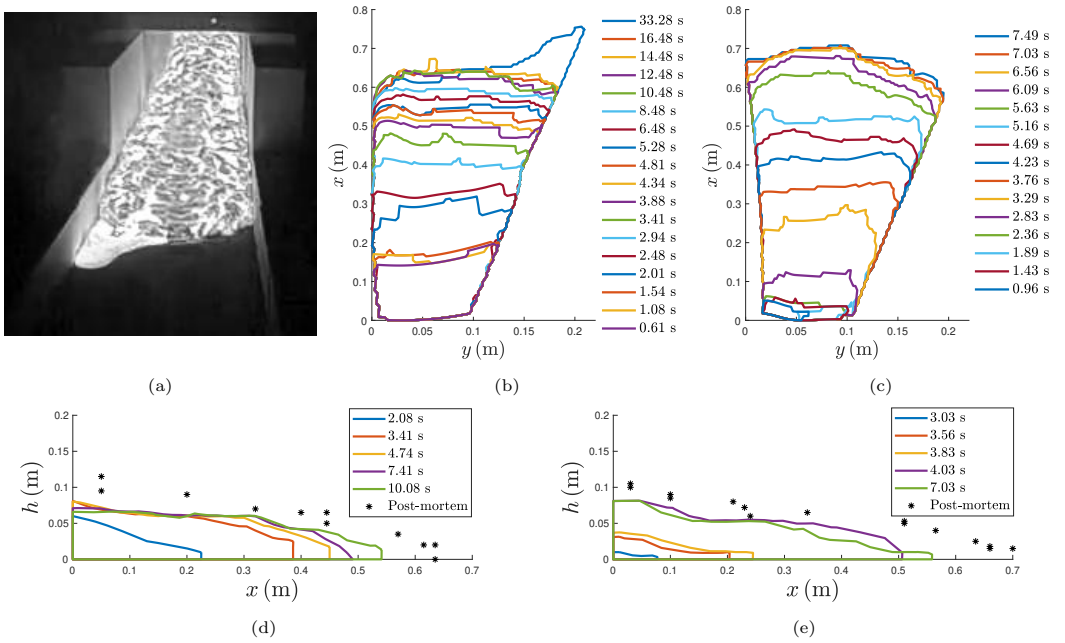

Figure 7. Image analysis of melt spreading including: (a) an example image from the VE-U9-ceramic test acquired from the Q1645 perspective, (b) a checkerboard calibration image of the spreading geometry, and contours of the propagating melt footprint (c-d) and profile (e-f) during the (c,e) VE-U9-ceramic and (d,f) VE-U9-concrete spreading tests. Note that the width and depth axes of the contour plots are magnified relative to the length axis for ease of visualization.

The observation that the front propagation time is comparable to the melt delivery time is consistent with gravity-viscous spreading, whereby additional melt supply is generally required to overcome the significant viscous resistance at the melt front and drive further spreading. While it remains possible that solidification increases the viscous resistance to flow within the timescale of spreading, it does not appear to be the case that solidification arrests the propagation of the melt front within the timescale of melt delivery into the channel.

Profiles of melt cross-section parallel to the flow were acquired from image analysis of the melt region in contact with the channel walls and are presented in Figure 7d-e. The uncertainty in melt depth measurements obtained by image analysis are considered to be ± 10 mm. The final melt profiles determined by image analysis appear shallower than the post-mortem measurements also shown in Figure 7d-e. This reflects the fact that image analysis extracts the melt depth adjacent to the wall, while the measurements acquired at the termination of the experiment correspond to the central axis of the melt, between the channel walls. The melt is slightly domed in topology due to friction at the vertical channel walls, resulting in a shallower profile in the immediate vicinity of the wall.

Video imaging of the spreading revealed a disparity in the motion of the two melts and in the evolution of the melt profiles, presented in Figure 7d-e. The VE-U9-concrete melt appears to glide over the sacrificial concrete substrate, indicative of reduced friction at the interface, in contrast with the VE-U9-ceramic test where the melt appears to crawl, consistent with considerable friction, or minimal slip, at the melt-substrate interface. The disparity in spreading motion is reflected in the melt topology, as noted during the post-experiment measurements of the depth profile. Figure 7e reveals a shallower melt profile at the melt front during the VE-U9-concrete test,

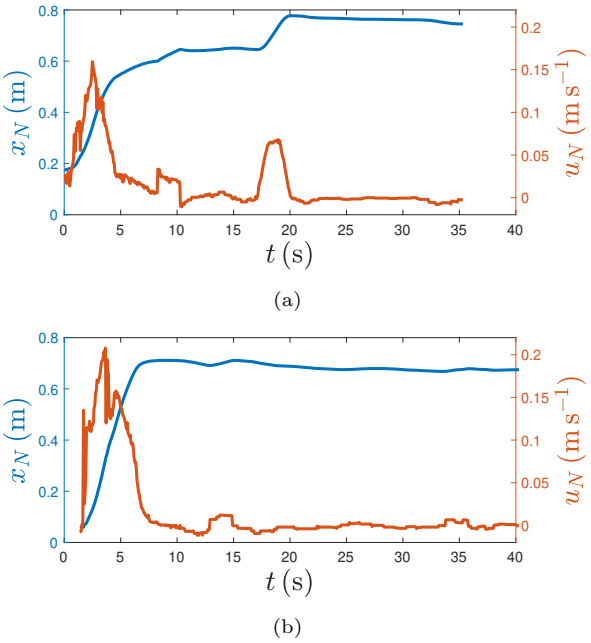

Figure 8. The evolution of spreading length and front velocity, averaged over 1 s intervals, with time during the (a) VE-U9-ceramic and (b) VE-U9-concrete spreading tests, as obtained from image analysis.

contrasting the more severe nose at the VE-U9-ceramic melt front. The alternative slip behaviour could be linked to the observation that the melt also appears to expand and contract in a series of porosity cycles during spreading on concrete, a phenomenon which was not observed during spreading on ceramic. These cyclical changes in porosity imply significant gas production as a result of the MCCI. This raises the possibility of a film of steam, gaseous concrete decomposition products and molten sacrificial concrete lubricating the melt-substrate interface. No such lubrication is possible during the VE-U9-ceramic test due to the inert interaction between the melt and the zirconia substrate.

The enhanced spreading on sacrificial concrete appears, at first glance, to conflict with the diminished spreading on classical concrete (relative to a ceramic substrate) observed during the VE-U7 test[19] or the KATS tests, where corium melts spread significantly further on ceramic than on conventional concrete[17], however these findings are not necessarily contradictory. Steam liberation from the concrete may enhance interfacial slip, but may also accelerate melt cooling, and thus viscous resistance to flow, due to the aforementioned sparging effect. The competition between these two effects will depend on many factors, not limited to (1) the initial melt temperature, (2) the duration of melt flow into the channel, (3) the roughness of the substrate surface, (4) the water content and composition of the concrete and (5) the energetics of the MCCI. As such, steam generation may augment or diminish the spreading potential depending on the initial conditions. While the existence of a lubricating film can be implied from the burn marks, ablation of the concrete and the spreading dynamics, it is not realistic to directly detect a vapour-molten concrete film at the interface from image analysis. The influence of the slip condition on the melt profile and front velocity will instead be investigated using numerical simulations in part 2 of this study.

Further analysis of the melt footprints in Figure 7c-d enabled the characterization of the evolution of the length, x_N, and velocity, u_N, of the melt front with time, as

presented in Figure 8 (the spreading length in this instance is taken to be the maximum distance from the centre of the channel entry to the melt front). The duration of front propagation does not appear to differ significantly between the two experiments. The initial period of spreading with a front velocity in excess of $0.03\,\mathrm{m\,s^{-1}}$ (lower velocities are potentially attributable to noise within the uncertainty limits of the image analysis) was 4.4 s on ceramic and 4.9 s on sacrificial concrete. The second spike in front velocity during the VE-U9-ceramic spreading test (from around 17 s) captures the formation of the melt tongue. The impression of a slight reduction in spreading length over time thereafter is an artefact of the image analysis. As the melt cools its luminosity diminishes and the contrast between the melt and substrate at the spreading front diminishes, resulting in increased uncertainty in the precise location of the spreading front.

The 7 % increase in spreading length on sacrificial concrete, as compared with ceramic, is accompanied by a 30 % increase in maximum front velocity. The increase in both maximum front velocity and spreading length on sacrificial concrete, in spite of the reduced mass and potentially increased viscosity during the VE-U9-concrete test, indicates a significantly enhanced spreadability on sacrificial concrete, and implies that the slip behavior at the melt-substrate interface may significantly influence the spreading dynamics. The extent to which the spreadability may be enhanced by the slip condition will be investigated quantitatively in part 2 of the study[26].

Nomenclature

T	temperature (K)
$\dot{m}$	mass flow rate ($\mathrm{kg\,s^{-1}}$)
ϵ	emissivity
μ	dynamic viscosity (Pa s)
ϕ	porosity
ρ	density ($\mathrm{kg\,m^{-3}}$)
h	melt depth (m)
i, j	image pixel coordinates
m	mass (kg)
t	time (s)
u	velocity ($\mathrm{m\,s^{-1}}$)
x, y, z	spreading coordinates (m)

Acronyms

MCCI	molten core-concrete interaction
RPV	reactor pressure vessel
SPECTRA	software for phase extraction and corium tracking analysis

Subscripts

air	air
c	closed
cr	crucible
eth	ethanol
L	liquidus
m	melt
N	melt front (nose)
o	open
res	resin
S	solidus
sp	spreading section
T	total

4. Conclusions

Image analysis of high-temperature corium spreading on ceramic and sacrificial concrete substrates revealed a 7 % increase in spreading length and a 30 % increase in maximum front velocity in the case of spreading on the sacrificial concrete. Significantly, these figures underestimate the disparity between spreading on the two sub-

strates since (1) the effective mass partaking in spreading was 18 % lower, and (2) thermal imaging indicated the melt to be around 45 °C lower in temperature during the spreading test on sacrificial concrete, which is estimated to correspond to a roughly three-fold increase in melt viscosity.

During the spreading test on sacrificial concrete, the melt appeared to expand and contract in a series of porosity cycles, which, combined with burn marks and localized ablation of the basemat to depths of 2–4 mm, indicates concrete decomposition, generating steam and hydrogen as well as molten concrete. The enhanced spreading on sacrificial concrete is best explained by enhanced slip at the melt-substrate interface due to the formation of a diphasic film of gaseous concrete decomposition products and molten concrete. The MCCI may therefore either enhance spreading by lubricating the melt-substrate interface, or diminish spreading by sparging the melt with ablation gases, increasing the rate of heat loss and enhancing the viscous resistance to spreading. The optimization of sacrificial concrete composition for core catcher designs should therefore balance these competing phenomena, maximizing the molten concrete viscosity while avoiding excessive gas production during the MCCI.

The two ≈ 30 kg-scale experiments reveal a number areas to be addressed by numerical simulation. A robust procedure is required to scale for differences in melt mass, porosity and viscosity during spreading experiments in this broadening channel geometry. The influence of alternative slip regimes at the melt-substrate interface on the spreading dynamics requires investigation. In addition, the influence of the physical and thermal hetereogeneity of the melts should be considered, since thermal imaging implied melt surface temperatures up to 100 °C lower at the spreading front than at the entry to the channel, potentially corresponding to an order of magnitude increase in viscosity over the spreading length. Further work is also required in the characterization of the thermophysical behavior of molten corium-concrete mixtures, in particular the viscosity between the solidus and liquidus temperatures and the emissivity in the infrared spectrum. The viscosity of the molten sacrificial concrete will require characterization for an improved understanding of the lubrication effects at the melt-substrate interface. Part 2 of this study[26] will present the derivation and application of scaling principles to quantify the impact of differences in mass flow rate, viscosity, density, porosity and the interfacial slip condition on the melt spreading dynamics in a broadening channel geometry.

5. Acknowledgements

The authors thank Mitsubishi Heavy Industries for funding the VE-U9 experiments in collaboration with the CEA. We also wish to thank the PLINIUS team for their management of the VULCANO facility during this experimental program.

References

[1] Journeau C, Haquet JF, Spindler B, et al. The VULCANO VE-U7 Corium spreading benchmark. Progress in Nuclear Energy. 2006;48(3):215–234.

[2] Dinh TN, Konovalikhin MJ, Sehgal BR. Core melt spreading on a reactor containment floor. Progress in Nuclear Energy. 2000;36(4):405–468.

[3] Yasumura Y, Yamaji A, Furuya M, et al. Investigation on influence of crust formation on VULCANO VE-U7 corium spreading with MPS method. Annals of Nuclear Energy. 2017;107:119–127.

[4] Sahboun N, Miwa S, Sawa K, et al. A molten metal jet impingement on a flat spreading surface. Journal of Nuclear Science and Technology. 2020;00(00):1–10.
[5] Fischer M, Henning A, Surmann R. Mitigation of severe accidents in AREVA's Gen 3+ nuclear power plants. Nuclear Engineering and Design. 2014;269:323–329.
[6] Huppert HE. The propagation of two-deminsional and axisymmetric viscous gravity currents over a rigid horizontal surface. Journal of Fluid Mechanics. 1982;121(121):43–58.
[7] Journeau C, Sudreau F, Gatt JM, et al. Thermal, physico-chemical and rheological boundary layers in multi-component oxidic melt spreads. International Journal of Thermal Sciences. 1999;38(10):879–891.
[8] Ramacciotti M, Journeau C, Sudreau F, et al. Viscosity models for corium melts. Nuclear Engineering and Design. 2001;204:377–389.
[9] Fink JH, Griffiths RW. Radial spreading of viscous-gravity currents with solidifying crust. Journal of Fluid Mechanics. 1990;221:485–509.
[10] Duan G, Yamaji A, Koshizuka S. A novel multiphase MPS algorithm for modeling crust formation by highly viscous fluid for simulating corium spreading. Nuclear Engineering and Design. 2019;343(January):218–231.
[11] Journeau C, Piluso P. Core concrete interaction. Vol. 2. Elsevier Inc.; 2012.
[12] Cognet G, Alsmeyer H, Tromm W, et al. Corium spreading and coolability: CSC Project. Nuclear Engineering and Design. 2001;209(1-3):127–138.
[13] Jubaidah, Duan G, Yamaji A, et al. Investigation on corium spreading over ceramic and concrete substrates in VULCANO VE-U7 experiment with moving particle semi-implicit method. Annals of Nuclear Energy. 2020;141:107266.
[14] Delacroix J, Chikhi N, Fouquart P, et al. Solidus and liquidus temperatures of corium - sacrificial material mixtures : experimental results and thermodynamic calculations. In: FDR2019 International Topical Workshop on Fukushima Decommissioning Research; May; Fukushima; 2019.
[15] Hartel C, Meiburg E, Necker F. Analysis and direct numerical simulation of the flow at a gravity-current head. Part 1. Flow topology and front speed for slip and no-slip boundaries. Journal of Fluid Mechanics. 2000;418:189–212.
[16] Suzuki H, Matsumoto T, Mitadera T, et al. Proceedings of the 2nd ASME-JSME Nuclear Engineering Joint Conference. American Society of Mechanical Engineers; 1993.
[17] Fieg G, Huber F, Werle H, et al. Simulation experiments on the spreading behavior of molten core melts. In: Proceedings of the National Heat Transfer Conference; Houston, Texas; 1996.
[18] Magallon D. The FARO program recent results and synthesis. In: Proceedings of CSARP Meeting, Bethesda (USA); Bethesda, Md; 1997.
[19] Journeau C, Boccaccio E, Brayer C, et al. Ex-vessel corium spreading: results from the VULCANO spreading tests. Nuclear Engineering and Design. 2003;223:75–102.
[20] Harris C, Stephens M. A combined corner and edge detector. In: Proceedings of the 4th Alvey Vision Conference; 1988. p. 147–151.
[21] Hughes TJ. The Finite Element Method: Linear Static and Dynamic Finite Element Analysis. Englewood Cliffs, New Jersey: Prentice-Hall, Inc.; 1987.
[22] Yang TY. Finite element structural analysis. Vol. 2. Prentice-Hall Englewood Cliffs, NJ; 1986.
[23] Watson D. Contouring: a guide to the analysis and display of spatial data. Elsevier; 2013.
[24] Johnson M, Journeau C, Matsuba K, et al. Annals of Nuclear Energy Characterization of high-temperature nuclear fuel-coolant interactions through X-ray visualization and image processing. Annals of Nuclear Energy. 2021;151:107881.
[25] Brissonneau L, Ikeuchi H, Piluso P, et al. Material characterization of the vulcano corium concrete interaction test with concrete representative of fukushima daiichi nuclear plants. Journal of Nuclear Materials. 2020 1;528.
[26] Johnson M, Schiano T, Denoix A, et al. High-temperature ex-vessel corium spreading. Part 2: Scaling principles for gravity-viscous spreading with slip at the melt-substrate interface. 2021;[Under review].

[27] Udalov YP, Pozniak IV, Sazavsky P, et al. Physicochemical transformations in multicomponent melts containing uranium, zirconium, and iron oxides and calcium silicates and aluminates. Russian Journal of Applied Chemistry. 2017;90(6):838–845.
[28] Shaw HR. Rheology of basalt in the melting range. Journal of Petrology. 1969; 10(November):510–535.

Appendix A. Porosity calculations

The mass of a sample measured in air and in a reference fluid of known density enables the estimation of the sample volume and thus the bulk density (both inclusive of closed pores). The bulk density and volume of the 'i' forms (or preparation methods) of each sample are given by:

$$\begin{aligned} \rho_i &= \frac{m_{i,air}}{m_{i,air} - m_{i,eth}}(\rho_{eth} - \rho_{air}) + \rho_{air} \\ V_i &= \gamma \frac{m_{i,air} - m_{i,eth}}{\rho_{eth} - \rho_{air}} \end{aligned} \tag{A1}$$

where γ is an adjustment coefficient for the electronic scales, equivalent to 0.99985. This approach enabled the density of four nickel samples to be estimated to within an accuracy of $\pm 0.06\,\%$.

The closed porosity is determined from the ratio of the bulk density of the melt, inclusive of the closed pore-space, to the density of the solid melt exclusive of porosity, $\phi_c = 1 - \rho_{m+c}/\rho_m$. The bulk density inclusive of closed porosity is simply that determined for the first form of the sample, $\rho_{m+c} = \rho_1$. The density of the solid melt exclusive of the porosity, ρ_m, is determined from the third form (milled and set in resin):

$$\rho_m = \frac{m_1 + V_1\rho_{air}}{\frac{m_1 + V_1\rho_{air} + m_{3,res}}{\rho_3} - \frac{m_{3,res}}{\rho_{res}}} \tag{A2}$$

Alternatively, the numerator $(m_1 + V_1\rho_{air})$ can be replaced by the mass of solidified melt determined for the milled sample prior to setting in resin, providing care is taken that negligible mass is lost between the mill and electronic scales. The densities inclusive and exclusive of the closed pores provide that:

$$\phi_c = 1 - \frac{\rho_1}{\rho_3}\left(1 + \frac{m_{3,res}}{m_1 + V_1\rho_{air}}\left(1 - \frac{\rho_3}{\rho_{res}}\right)\right) \tag{A3}$$

The open porosity, ϕ_o, is then determined from the estimated closed porosity and the density analysis of forms 1 and 2, representing the sample before and after impregnation with resin. The ratio of the open porosity to the solid fraction of the sample prior to impregnation with resin, $\phi_m = 1 - \phi_c - \phi_o$, is estimated by:

$$\frac{\phi_o}{\phi_m} = \frac{\phi_o}{1-\phi_c-\phi_o} = \frac{\rho_1 - \frac{\rho_2}{1-\phi_c}}{\rho_2 - \rho_{res}} \tag{A4}$$

The open porosity is thus given by:

$$\phi_o = \frac{\frac{\phi_o}{\phi_m}}{1+\frac{\phi_o}{\phi_m}}(1-\phi_c) = \frac{\rho_1(1-\phi_c)-\rho_2}{\rho_1 - \rho_{res} - \rho_2\left(\frac{\phi_c}{1-\phi_c}\right)} \tag{A5}$$

The uncertainty of this approach diminishes when there is clear contrast between the density of the impregnated sample and the resin, $\rho_2 - \rho_{res} \gg 0$, which was favorable in this instance as the solid melt densities in the order of 6.3–7.2 $\mathrm{g\,cm^{-3}}$ are 5–6 times greater than the resin density of 1.15 $\mathrm{g\,cm^{-3}}$.